JACS
JOURNAL OF THE AMERICAN CHEMICAL SOCIETY
pubs.acs.org/JACS
Article

Catalytic Reduction of Dioxygen to Water by a Bioinspired Non-Heme Iron Complex via a 2+2 Mechanism

Emma N. Cook, Diane A. Dickie, and Charles W. Machan*

Cite This: https://doi.org/10.1021/jacs.1c04572
Read Online

ABSTRACT: We report a bioinspired non-heme Fe complex with a tripodal $[N_3O]^-$ ligand framework ($Fe(PMG)(Cl)_2$) that is electrocatalytically active toward dioxygen reduction with acetic acid as a proton source in acetonitrile solution. Under electrochemical and chemical conditions, $Fe(PMG)(Cl)_2$ selectively produces water via a 2+2 mechanism, where H_2O_2 is generated as a discrete intermediate species before further reduction to two equivalents of H_2O. Mechanistic studies support a catalytic cycle for dioxygen reduction where an off-cycle peroxo dimer species is the resting state of the catalyst. Spectroscopic analysis of the reduced complex $Fe^{II}(PMG)Cl$ shows the stoichiometric formation of an Fe(III)-hydroxide species following exposure to H_2O_2; no catalytic activity for H_2O_2 disproportionation is observed, although the complex is electrochemically active for H_2O_2 reduction to H_2O. Electrochemical studies, spectrochemical experiments, and DFT calculations suggest that the carboxylate moiety of the ligand is sensitive to hydrogen-bonding interactions with the acetic acid proton donor upon reduction from Fe(III)/(II), favoring chloride loss *trans* to the tris-alkyl amine moiety of the ligand framework. These results offer insight into how mononuclear non-heme Fe active sites in metalloproteins distribute added charge and poise proton donors during reactions with dioxygen.

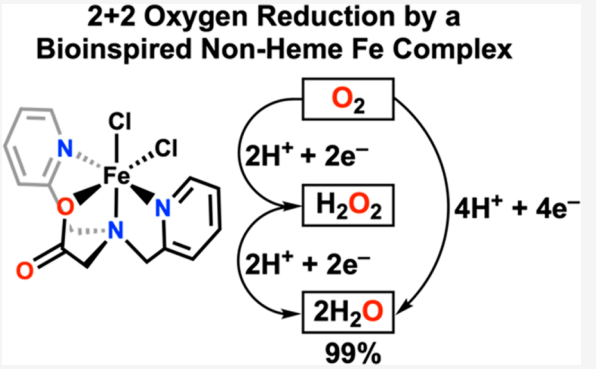

INTRODUCTION

The oxygen reduction reaction (ORR) plays important roles in both biological energy conversion and next-generation energy technologies.[1−6] Selectivity for the two-proton−two-electron ($2H^+/2e^-$) product, H_2O_2, is attractive as a direct route to an important chemical oxidant.[1,7] The alternative $4H^+/4e^-$ product, H_2O, is an ideal half-reaction for fuel cell applications, where it enables the coupled electrochemical oxidation of energy-rich fuels.[1] This is analogous to the use of O_2 in many bioinorganic systems, where O_2 reduction drives chemical oxidation reactions. Additionally, the ORR can proceed via a 2+2 mechanism, where the $2H^+/2e^-$ reduction of O_2 to H_2O_2 is followed by an additional $2H^+$ and $2e^-$ to generate two equivalents of H_2O.[1] An understanding of what controls O_2 activation, reduction, and ORR selectivity at well-defined metal active sites remains an important question.

Platinum has traditionally been the best catalyst for the ORR, but due to its high cost and limited reserves, low-cost and earth-abundant transition metal catalysts are needed.[5] Stemming from continuous efforts to mimic biological active sites for O_2 storage, transport, and activation, macrocyclic N_4 complexes with iron,[8,9] cobalt,[10,11] and manganese[12,13] active sites have been studied extensively as molecular catalysts for the ORR.[1,14−18] Non-macrocyclic ligand frameworks have been relatively less explored, with limited reports on cobalt-,[19,20] copper-,[21,22] and manganese-based[23−25] systems.[1] To the best of our knowledge, there has only been one previously reported homogeneous non-macrocyclic iron system shown to be a competent catalyst for the ORR.[26] In 2019, Wang et al. reported an iron(II) thiolate dinuclear complex that was an efficient ORR catalyst whose selectivity shifted from H_2O_2 (∼95%) under chemical conditions to H_2O (less than ∼10% H_2O_2) under electrochemical conditions.[26] It is also worth noting that an electrode-deposited molecular non-heme iron catalyst for the ORR has been reported previously.[27]

Despite the focus on Fe heme-based molecular ORR catalysts, there are abundant examples of non-heme Fe metalloenzymes that activate dioxygen.[28−32] For example, iron dioxygenases catalyze the oxidative cleavage of catechols during the degradation of natural aromatics.[29] The inner coordination sphere of this active site contains histidine residues and an anionic carboxylate moiety.[29,33,34] Synthetic models of dioxygenase active sites have been developed using a

Received: May 2, 2021

https://doi.org/10.1021/jacs.1c04572
J. Am. Chem. Soc. XXXX, XXX, XXX−XXX

variety of tripodal ligand frameworks to study O_2 activation and reactivity with catechol.[29,35−39] However, we are unaware of demonstrated catalytic activity toward the ORR with these activity and structural models. Interestingly, homologous mononuclear Fe active sites are also observed in Fe superoxide dismutase, lipoxygenase, pterin-dependent hydroxylases, α-keto acid-dependent enzymes, and isopenicillin N synthase.[29,40]

A $[N_3O]^-$ tripodal ligand framework provides an anionic O group in the inner-coordination sphere, which can act as a Lewis base, and two open coordination sites in the axial and equatorial positions that allow for substrate binding.[38] Using a $[N_3O]^-$ ligand that mimics the inner-coordination sphere of the metalloenzymes described above, we show that the non-heme Fe(III) complex $Fe(PMG)(Cl)_2$ electrocatalytically reduces O_2 to water through a 2+2 mechanism with quantitative efficiency. Further, a component of catalyst activation during reduction is a noncovalent interaction between acetic acid and the carboxylate moiety, suggesting that distribution of added charge and proton equivalents between the metal center and ligand framework is essential to the observed activity.

RESULTS

Synthesis and Characterization. *N,N′*-Bis(2-pyridylmethyl)glycine (PMG(H)) was synthesized using a previously reported procedure.[41] Under basic conditions, a solution of glycine and two equivalents of 2-(chloromethyl)-pyridine hydrochloride was allowed to stir at room temperature for 5 days. Metalation of PMG(H) to generate Fe(*N,N′*-bis(2-pyridylmethyl)glycine)$(Cl)_2$ ($Fe(PMG)(Cl)_2$) was achieved after 24 h under reflux conditions in ethanol with a stoichiometric amount of iron(III) chloride hexahydrate. UV−vis and NMR spectroscopies, as well as ESI-MS and microanalysis (see SI), are consistent with the crystallographically determined structure of the Fe complex shown in Figure 1. Evans' method measurements in methanol (MeOH) exhibited a μ_{eff} of 5.64 ± 0.05, consistent with a high-spin d^5 Fe(III) complex.[42,43]

Electrochemical Studies with O_2. Cyclic voltammetry (CV) experiments were performed on $Fe(PMG)(Cl)_2$ in a solution of 0.1 M tetrabutylammonium hexafluorophosphate ($TBAPF_6$) in acetonitrile (MeCN). A single quasi-reversible feature is observed at $E_{1/2}$ = −0.44 V vs Fc^+/Fc (Figure 2, black trace), which is attributed to the Fe(III)/(II) reduction. This reduction feature shows a proton donor-dependent voltage response where titrating acetic acid (AcOH) into the solution shows a shift to more positive potentials (Figure 2, blue trace). Plotting the $E_{1/2}$ values against log[AcOH] exhibits a 127 mV/log [AcOH] dependence (Figure S6). Although Nernstian responses can be consistent with a proton-coupled electron transfer (PCET) process,[23,44,45] control studies suggest that formal proton transfer does not occur under these conditions. We conducted analogous electroanalytic studies with a control complex containing a neutral ligand framework (tris-pyridylamine = TPA), $[Fe(TPA)(Cl)_2][Cl]$, whose structure is similar to a previously reported Fe(II) complex.[46] In MeCN solution, a reversible Fe(III)/(II) redox feature at −0.20 V vs Fc^+/Fc is observed under Ar saturation conditions, which shows a proton donor-dependent voltage response: titrating AcOH shows a 91 mV/log [AcOH] dependence (Figure S7). These data suggest that addition of AcOH aids in Cl^- dissociation. However, the steeper voltage dependence of $Fe(PMG)(Cl)_2$ on [AcOH] is suggestive of additional interactions, which we propose involve hydrogen-bonding interactions with the anionic carboxylate group, *vide infra*.

Under O_2 saturation conditions the Fe(III)/(II) reduction feature of complex **1** becomes completely irreversible (Figure 2, red trace), indicative of O_2 binding to the reduced metal center via an EC mechanism.[47,48] To ensure that the observed loss of reversibility was not attributed to delayed Cl^- loss, variable scan rate studies were performed from 20 to 100 mV/s under Ar saturation conditions (Figure S8). These data suggest chloride-loss kinetics are slow on the CV time scale and that irreversibility is driven by thermodynamically favorable O_2 binding to Fe(II). In the presence of AcOH as an added proton donor, there is an increase in current at the Fe(III)/(II) reduction feature, consistent with electrocatalytic activity

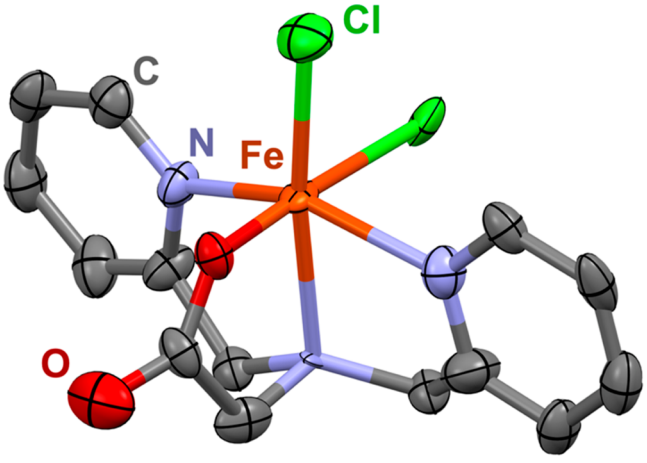

Figure 1. Molecular structure of $Fe(PMG)(Cl)_2$ from single-crystal X-ray diffraction studies. Orange = Fe, green = Cl, red = O, blue = N, gray = C; H atoms omitted for clarity; ellipsoids at 50%.

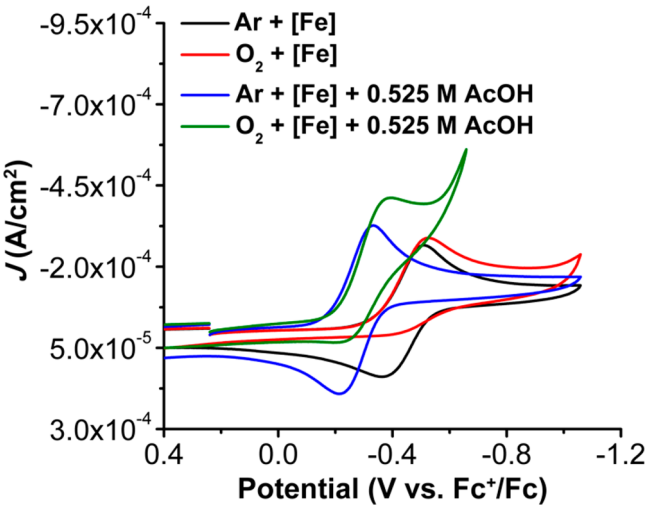

Figure 2. CVs of $Fe(PMG)(Cl)_2$ under Ar (black) saturation with 0.525 M AcOH (blue) and O_2 (red) saturation with 0.525 M AcOH (green). Conditions: 1 mM $Fe(PMG)(Cl)_2$, 0.1 M $TBAPF_6$ in MeCN; glassy carbon working electrode; Ag/AgCl pseudoreference electrode; scan rate 100 mV/s; referenced to internal ferrocene standard.

https://doi.org/10.1021/jacs.1c04572
J. Am. Chem. Soc. XXXX, XXX, XXX−XXX

toward O_2 reduction (Figure 2, green trace). Subsequently, second-order rate constants for O_2 binding under aprotic (k_{O2}) and protic ($k_{O2,H+}$) conditions were determined using the evolution of the observed peak potential with respect to changes in scan rate, as previously described by Dempsey and co-workers.[47,49] The rate constant, k_{O2}, was determined to be 14.5 ± 3.6 M^{-1} s^{-1} and $k_{O2,H+}$ = 6.12 ± 0.96 M^{-1} s^{-1} with 0.525 M AcOH (see SI). The decrease from aprotic to protic conditions indicates that O_2 binding is sensitive to the reducing power of the Fe center in a Tafel-dependent manner. Rotating ring-disk electrode methods were used to determine that Fe(PMG)$(Cl)_2$ demonstrated 25 ± 10% selectivity for H_2O_2 under electrochemical ORR conditions with 0.35 M AcOH present (see SI).

To analyze the proton-donor dependence and take into account homoconjugation of AcOH in MeCN ($\log(K_{AHA})$ = 3.9),[50] CVs were subsequently taken under buffered conditions. Addition of 1:1 tetrabutylammonium acetate (TBAAcO)−AcOH resulted in a negative potential shift of 190 mV in the Fe(III)/(II) reduction feature (Figure S12), indicative of acetate binding as a ligand to the Fe metal center and implying the formation of a new Fe(III) species. Spectrochemical evaluation of ORR catalysis under buffered conditions showed a significantly slower rate in comparison to nonbuffered conditions (Figure S30). We propose that the observed decrease in activity is the result of superior binding of acetate to the Fe center following reduction to the formally Fe(II) state. As a result of this inhibition the the effective overpotentials given below for nonbuffered conditions are corrected using the reported homoconjugation value for AcOH in MeCN, however, these values should be considered as a lower-limit estimation (see SI).[51]

Spectrochemical Studies with O_2. Catalytic ORR experiments with Fe(PMG)$(Cl)_2$ were run under spectrochemical conditions using decamethylferrocene (Cp^*_2Fe) as a chemical reductant. UV−vis stopped-flow spectroscopy was used to determine the kinetic parameters of the ORR based on the rate of $[Cp^*_2Fe]^+$ appearance under O_2 saturation conditions with AcOH present in MeCN (eq 1, Figure 3),

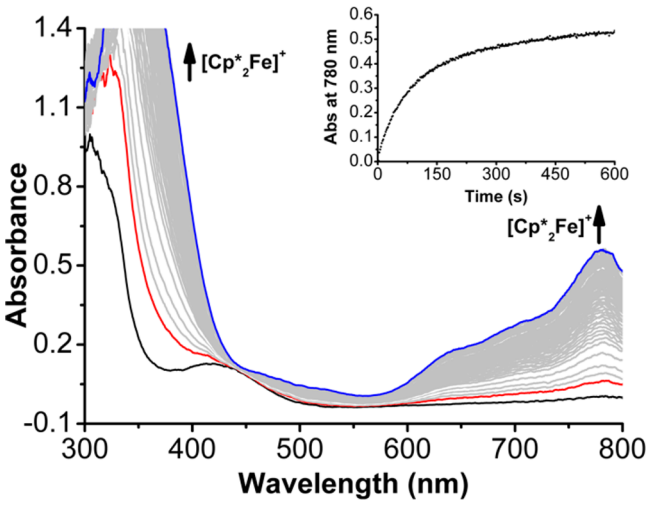

Figure 3. Representative UV−vis spectral changes under catalytic conditions in MeCN over 15 min. Concentrations: 50 μM Fe(PMG)$(Cl)_2$, 35 mM AcOH, 4.05 mM O_2, and 1.5 mM Cp^*_2Fe. Inset: Absorbance changes at 780 nm arise from the formation of $[Cp^*_2Fe]^+$.

where under the same reaction conditions without Fe(PMG)$(Cl)_2$, the system shows negligible background reactivity (Figure S29). Variable-concentration studies were used to elucidate the catalytic rate law of the ORR by Fe(PMG)$(Cl)_2$, which showed zero-order dependencies on [AcOH], $[Cp^*_2Fe]$, and $[O_2]$. Conversely, a half-order dependence was observed on $[Fe(PMG)(Cl)_2]$ (eq 2, Figures S20−S23). The turnover frequency (TOF) was determined to be 0.92 s^{-1} with 35 mM AcOH (overpotential (η) = 0.15 V, see SI). As mentioned above, the lack of activity under buffered conditions precludes us from being able to accurately calculate overpotential. We have corrected the reported standard reduction potentials for the ORR, as outlined in the SI, to take into account the pK_a (23.5) and $\log(K_{AHA})$ (3.9) values for AcOH in MeCN.[1,50,51] We emphasize here that our calculation of overpotential is a *lower-limit approximation*.

$$O_2 + 4Cp^*_2Fe + 4AcOH \xrightarrow{Fe} 2H_2O + 4[Cp^*_2Fe]^+ + 4AcO^- \quad (1)$$

$$\text{rate} = k_{cat}[Fe]^{0.5}[AcOH]^0[O_2]^0[Cp^*_2Fe]^0 \quad (2)$$

Selectivity for the ORR determined via a Ti(O)SO_4-based colorimetric assay showed the system had a H_2O_2 selectivity of only 1.1 ± 2%, which is less than the 25% H_2O_2 selectivity under electrochemical conditions.[52] Notably, control experiments indicated that no H_2O_2 disproportionation occurred over the course of 30 min when Fe(PMG)$(Cl)_2$, AcOH, and urea·H_2O_2 were combined under Ar gas saturation conditions (Figure S18). However, placing Fe(PMG)$(Cl)_2$ under anaerobic conditions with Cp^*_2Fe in addition to added acid and urea·H_2O_2 showed rapid reduction of H_2O_2 to H_2O with quantitative efficiency. We attribute the difference in observed selectivity under electrochemical and spectrochemical conditions to the time scale of each experiment. In a typical spectrochemical product quantification experiment, the reaction is run to completion with respect to the amount of O_2 present (~15 min) in the presence of excess Cp^*_2Fe and AcOH, which allows for any H_2O_2 produced during catalysis to be further reduced by Fe(PMG)$(Cl)_2$. However, in a typical RRDE experiment, catalysis occurs at the glassy carbon disk and H_2O_2 produced during catalysis is rapidly (~1 s) swept away from where catalytically active Fe(II) is generated, preventing further reduction. Consistent with this, control experiments show no catalytic activity for disproportionation of H_2O_2 mediated by Fe(PMG)$(Cl)_2$ (Figure S18), although stoichiometric oxidation of the singly reduced Fe^{II}(PMG)Cl complex is observed, *vide infra*. Overall, these data support a ~99% selectivity toward water, corresponding to the consumption of n_{cat} = 3.98 electrons per catalyst turnover and implicate a 2+2 mechanism, where H_2O_2 is a discrete intermediate. Variable-temperature stopped-flow spectroscopic data were used for Eyring analysis of the ORR catalyzed by Fe(PMG)$(Cl)_2$ (Table 1, Figure S32), which revealed a barrier for the rate-determining step (RDS) at 298 K of 20.5 kcal mol^{-1}, which is consistent with the observed TOF of 0.92 s^{-1}.

The reduction of H_2O_2 to H_2O under spectrochemical conditions was also studied using UV−vis stopped-flow spectroscopy, revealing relatively faster rates than the ORR catalyzed by Fe(PMG)$(Cl)_2$ (eq 3, Figure 4). Variable-concentration studies under anaerobic conditions revealed a rate of H_2O_2 reduction that has first-order dependencies on

https://doi.org/10.1021/jacs.1c04572
J. Am. Chem. Soc. XXXX, XXX, XXX−XXX

Table 1. Eyring Parameters of O_2 Reduction with $Fe(PMG)(Cl)_2$ from Variable-Temperature Spectrochemical Experiments

$\Delta H^{\ddagger}$	4.82 kcal mol^{-1}
$\Delta S^{\ddagger}$	−52.5 cal mol^{-1} K^{-1}
$\Delta G^{\ddagger}_{298\ K}$	20.5 kcal mol^{-1}

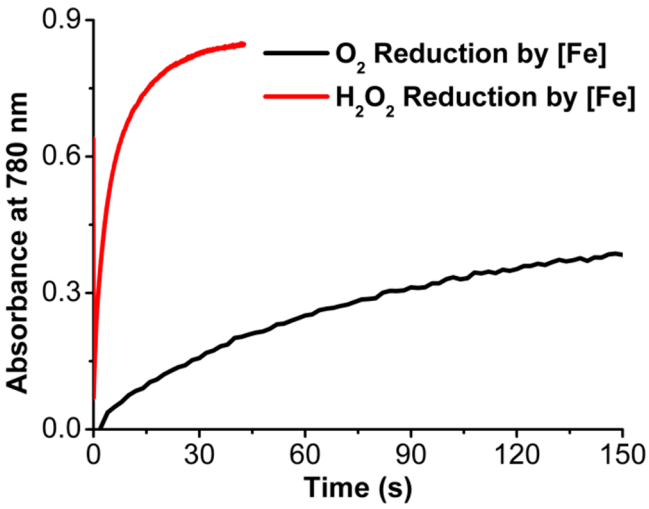

Figure 4. Absorbance changes at 780 nm due to the formation of $[Cp^*_2Fe]^+$ during O_2 (black) and H_2O_2 (red) reduction catalyzed be $Fe(PMG)(Cl)_2$. Conditions: (black) 50 μM [$Fe(PMG)(Cl)_2$], 35 mM [AcOH], 1.50 mM [Cp^*_2Fe], 4.05 mM O_2 (red) 50 μM [$Fe(PMG)(Cl)_2$], 35 mM [AcOH], 1.50 mM Cp^*_2Fe, 4 mM urea·H_2O_2.

[$Fe(PMG)(Cl)_2$] and [AcOH]. Conversely, zero-order dependencies on [Cp^*_2Fe] and [H_2O_2] are observed under the same conditions (eq 4, Figures S24–S27), and the TOF was determined to be 2.9 × 10^3 s^{-1} (η = 0.74 V, see SI). Notably, the Cp^*_2Fe is required to be present in solution for any consumption of H_2O_2 to occur (Figure S18). As before, this overpotential is determined by correcting the standard potential for the homoconjugation of AcOH and is a *lower-limit approximation*.

$$H_2O_2 + 2Cp^*_2Fe + 2AcOH \xrightarrow{Fe} 2H_2O + 2[Cp^*_2Fe]^+ + 2AcO^- \quad (3)$$

$$\text{rate} = k_{cat}[Fe]^1[AcOH]^1[H_2O_2]^0[Cp^*_2Fe]^0 \quad (4)$$

Electrochemical Studies with H_2O_2. CV studies were also performed with $Fe(PMG)(Cl)_2$ in the presence of H_2O_2 with AcOH under an inert atmosphere (Ar). Addition of urea·H_2O_2 to a solution of $Fe(PMG)(Cl)_2$ resulted in the loss of reversibility of the Fe(III)/(II) feature, indicative of the formation of an irreversible reaction between Fe(II) via a noncatalytic EC mechanism (Figure 5, red trace).[47,48] The evolution of observed peak potential with respect to changes in scan rate was used to determine the second-order rate constant for H_2O_2 binding, as previously described.[47,49] The rate constant, k_{H2O2}, was determined to be 1.52 ± 0.16 × 10^3 M^{-1} s^{-1} (see SI) and is consistent with the difference in O_2 and H_2O_2 reduction rates observed under spectrochemical conditions (Figure 4). Spectroscopic studies described below indicate that the primary product of this stoichiometric EC reaction is an Fe(III)–OH species. Complex **1** is electrocatalytically active toward H_2O_2 reduction in the presence of AcOH, with an appreciable increase in current density at the Fe(III)/(II) redox feature (Figure 5, green trace), consistent with the spectrochemical data discussed above. Overall, the spectrochemical and electrochemical data suggest that the Fe(III) state of the precatalyst $Fe(PMG)(Cl)_2$ does not appreciably react with H_2O_2.

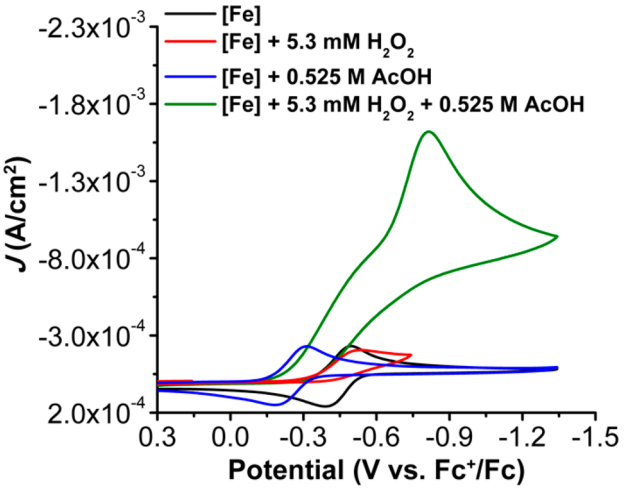

Figure 5. CVs of $Fe(PMG)(Cl)_2$ under Ar (black) saturation with 5.3 mM urea·H_2O_2 (red), 0.525 M AcOH (blue), and 0.525 M AcOH in the presence of 5.3 mM urea·H_2O_2 (green). Conditions: 1 mM $Fe(PMG)(Cl)_2$, 0.1 M $TBAPF_6$ in MeCN; glassy carbon working electrode; Ag/AgCl pseudoreference electrode; scan rate 100 mV/s; referenced to internal ferrocene standard.

Spectroscopic Studies with $Fe^{II}(PMG)Cl$. To better probe reaction intermediates, we directly prepared the catalytically active Fe(II) species ($Fe^{II}(PMG)Cl$) under anaerobic conditions and undertook UV–vis and ^{1}H NMR spectroscopic studies in MeCN in the presence of O_2, H_2O_2, and AcOH. First, we analyzed the role of the reduced Fe(II) in hydrogen-bonding with AcOH during catalysis. Titrating increasing amounts of AcOH to a sample of $Fe(PMG)(Cl)_2$ shows minimal spectral changes. However, adding AcOH to $Fe^{II}(PMG)Cl$ shows distinct increases in absorbance at 260, 325, and 365 nm, indicative of an interaction between AcOH and $Fe^{II}(PMG)Cl$ (Figure S34). UV–vis spectroscopic studies revealed that exposure of $Fe^{II}(PMG)Cl$ to O_2 at room temperature resulted in the formation of a new stable species after 8 min (Figure S36). To assess if this species corresponded to the proposed dimeric Fe species, we next titrated increasing amounts of urea·H_2O_2 to a 50 μM solution of $Fe^{II}(PMG)Cl$; clean isosbestic points were observed and changes in the UV–vis spectrum associated with the Fe(II) complex saturated at a 1:1 ratio of $Fe^{II}(PMG)Cl$ to H_2O_2 (Figure S37). During this titration, a band of relatively low absorptivity at 409 nm decreases in intensity, accompanied by the appearance of a new feature at 365 nm, with corresponding increases in absorbance features at 327 and 259 nm (Figure 6).

Molar absorptivity plots comparing the species produced when $Fe^{II}(PMG)Cl$ was exposed to O_2 and H_2O_2 with $Fe(PMG)(Cl)_2$ indicate a loss of all Fe(II) features with O_2 and H_2O_2 (Figure 6). These data suggest formation of an Fe(III) species; however, the spectral features following O_2 and H_2O_2 exposure do not match those of an authentic sample of $Fe(PMG)(Cl)_2$, which we propose is consistent with the absence of one of the chloride ligands. To assess alternate

https://doi.org/10.1021/jacs.1c04572
J. Am. Chem. Soc. XXXX, XXX, XXX–XXX

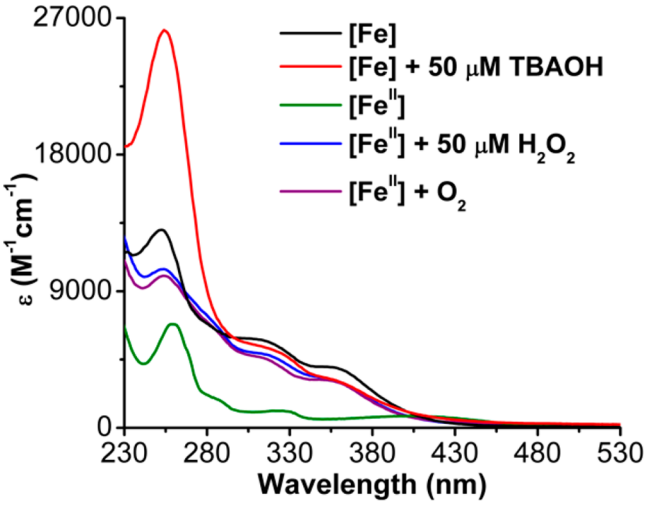

Figure 6. Molar extinction plot of 50 μM Fe(PMG)$(Cl)_2$ (black trace) exposed to 50 μM TBAOH and 50 μM Fe^{II}(PMG)Cl (green trace) exposed to 50 μM urea·H_2O_2 (blue trace) and O_2 (purple trace) in MeCN.

possibilities for the primary coordination environments in the Fe(III) species generated, we exposed a sample of Fe(PMG)-$(Cl)_2$ to tetrabutylammonium hydroxide (TBAOH). Overlays of Fe(PMG)Cl_2 with and without added TBAOH with Fe^{II}(PMG)Cl exposed to O_2 and H_2O_2 show good agreement, indicating that the product mixture likely contains stable Fe(III)−OH species (Figure 6). Since the kinetic data obtained in the mechanistic experiments imply the existence of an off-cycle dimer species, the formation of the same Fe(III)−OH species obtained from these two reactions suggests that the presumptive diiron peroxo dimer intermediate is reactive under experimental conditions, scavenging adventitious protons or H atom equivalents.

To supplement these data, we next analyzed the reactivity of Fe^{II}(PMG)Cl with AcOH using ^{1}H NMR spectroscopy. The paramagnetic ^{1}H NMR spectrum of Fe^{II}(PMG)Cl under N_2 showed six well-resolved broad resonances, indicative of a complex with a plane of internal symmetry (Figure S39). The addition of 0.3 M AcOH under N_2 showed changes consistent with the loss of the initial symmetry of Fe^{II}(PMG)Cl with 10 total paramagnetic resonances observed (Figure S40), which we ascribe to a hydrogen-bonded adduct of AcOH and the Fe(II) complex, as was previously demonstrated by comparable UV−vis (Figure S34) and electrochemical data (Figure 2). Exposure of Fe^{II}(PMG)Cl to H_2O_2 and O_2 showed a loss of all resolved paramagnetic features, precluding us from being able to characterize the Fe(III)−OH species via ^{1}H NMR.

DFT Calculations. To better understand the role of noncovalent interactions in facilitating chloride loss and the observed shift in the Fe(III)/(II) redox couple, we examined the thermodynamic positioning of reaction pathways involving Fe(PMG)$(Cl)_2$ (complex **1**), AcOH, MeCN, and the chloride anion before and after one-electron reduction using DFT methods (see SI). Note that this level of theory accurately replicated the sextet ground state of the complex observed experimentally; for brevity only the lowest energy spin configuration will be discussed, although alternative pathways have also been computed (see Computational Coordinates). From complex **1**, chloride loss is endergonic: *trans* to the trialkyl amine fragment of the ligand +13.8 kcal/mol, *trans* to the carboxylate +10.1 kcal/mol. Subsequent binding of MeCN is exergonic in both cases; however, the net displacement of chloride by MeCN is at least 8.0 kcal/mol endergonic (Figure 7). The introduction of AcOH in a noncovalent interaction

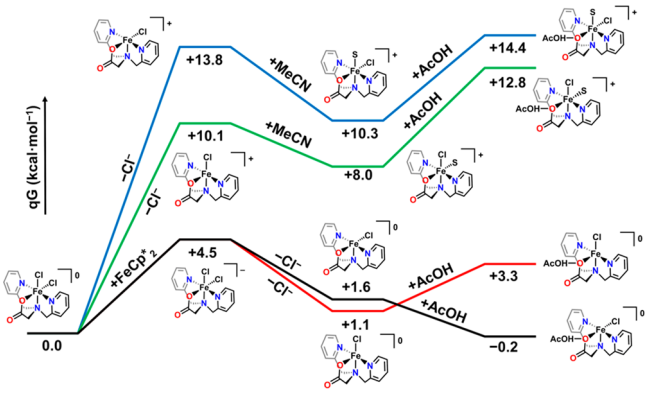

Figure 7. Computed reaction pathways comparing the effects of reduction and AcOH on chloride loss and MeCN binding. All Fe(III) species are S = 5/2; all Fe(II) species are S = 2; alternative spin configurations were higher in energy.

with the Fe-bound carboxylate is at least 4 kcal/mol endergonic in both cases. Alternative mechanistic pathways for the ordering of these three reaction steps were all higher in energy.

A lower energy pathway when complex **1** first undergoes a redox reaction with the Cp^*_2Fe reductant in solution (+4.5 kcal/mol). This reduction produces a formally Fe(II) species, which is most stable in the S = 2 spin manifold; alternate spin configurations were higher in energy. Chloride loss then becomes exergonic at both the possible positions (Figure 7, red and black); however AcOH binding is only favorable when chloride loss occurs in the position *trans* to the trialkylamine moiety of the ligand framework (Figure 7, black). For both of the reduction-first pathways, MeCN binding is slightly endergonic (+2.7 kcal/mol from the final species in the black pathway, Figure 7; +0.6 kcal/mol for the red). Formal protonation instead of MeCN binding is also thermodynamically disfavored in these noncovalent adducts by at least 4.2 kcal/mol, and solvento speciation does not help the favorability of the formal protonation reaction. Therefore, the lowest energy species in solution following one-electron reduction is five-coordinate, with a vacant coordination site opposite the trialkylamine. Noncovalent interactions between the five-coordinate neutral Fe species and AcOH increase the thermodynamic favorability of the chloride-loss reaction. Alternative sequences for reduction, chloride loss, and AcOH binding all produced higher-energy pathways.

DISCUSSION

Based on combined electrochemical and spectrochemical data, we can propose a mechanism for the ORR catalyzed by Fe(PMG)$(Cl)_2$, Scheme 1. Starting from **1**, a thermodynamically favorable noncovalent interaction between the anionic carboxylate group of the ligand in the inner coordination sphere and AcOH drives Cl^- loss following the formal reduction of the Fe(III) metal center to an Fe(II) species to form intermediate **2**. This proposal is supported indirectly by the sensitivity of the Fe(III)/(II) redox feature to added AcOH and directly by UV−vis spectroscopic data obtained

https://doi.org/10.1021/jacs.1c04572
J. Am. Chem. Soc. XXXX, XXX, XXX−XXX

Scheme 1. Proposed Catalytic Cycle for the ORR Catalyzed by Fe(PMG)(Cl)$_2$

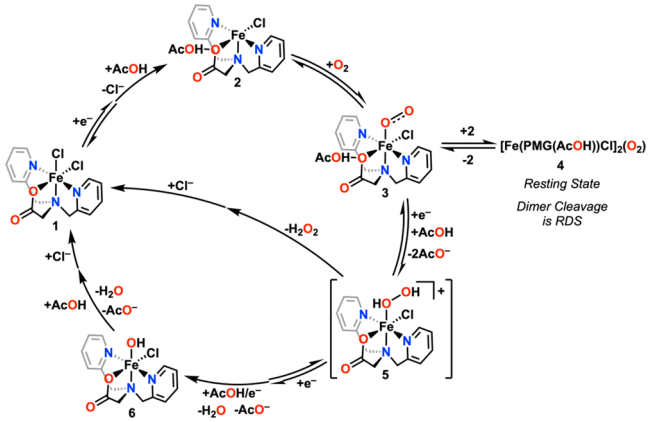

during the titration of AcOH into solutions with Fe(PMG)-(Cl)$_2$ and Fe^{II}(PMG)Cl, showing a distinct interaction for the Fe(II) complex (Figure S34). Consistent with this interpretation, paramagnetic ^{1}H NMR data show a loss of internal symmetry for the Fe(II) species, Fe^{II}(PMG)Cl, when AcOH is added (Figure S40). These experimental data are supported by DFT studies, which suggest chloride loss occurs opposite the trialkyl amine fragment of the ligand.

From this five-coordinate neutral species, we propose that O_2 binds to the Fe(II) metal center to form a mononuclear superoxo species, **3**. Using variable scan rate electrochemical experiments, a second-order rate constant of $k_{O2,H+}$ = 6.12 ± 0.96 M^{-1} s^{-1} is obtained with AcOH present for this reaction. From this intermediate it is likely a second equivalent of **2** reacts with an equivalent of **3** to form a bridging peroxo species, **4**, which we propose to be the resting state of the catalyst in solution. This assignment of an off-cycle dimer is based on the mechanistic kinetic analysis of this catalyst system described above, where the reaction has a half-order concentration dependence on the Fe-based catalyst precursor, eq 2. Off-cycle dimers have been previously reported for other systems and were likewise observed to have a half-order concentration dependence with respect to catalyst.[53,54] Based on literature precedent, we speculate that a μ_2-1,2-peroxo coordination mode is a likely possibility,[55−57] although we note the reactivity of this species has precluded direct characterization. As described above, the only stable product observed in exposing Fe^{II}(PMG)Cl to O_2 is an Fe(III)−OH species, suggesting the proposed intermediate O_2 dimer decomposes (Figure 6).

The rate-determining step of the catalytic cycle is proposed to be the cleavage of an Fe(III)−O bond to re-form an equivalent of **3** and an equivalent of **2**. Complex **3** can then undergo further reduction and coupled protonation to form an unobserved hydrogen peroxide-containing intermediate, **5**. To explore an alternative on-cycle dimer cleavage pathway, a kinetic study under standard ORR conditions varying [Fe-(PMG)Cl$_2$] concentration in the presence of 1 mM tetrabutylammonium chloride (TBACl) was conducted, to probe the possibility of chloride coordination accelerating peroxo dimer cleavage (Figure S31). However, the observed R_{fit}/n_{cat} dependence is slightly shallower than data obtained without TBACl present, indicating a slight inhibition of the catalytic response. These data are not consistent with Cl^- association mediating rate-limiting dimer cleavage.

At this point, unobserved intermediate **5** can then release H_2O_2. UV−vis experiments with complex **1** show no interaction between H_2O_2 and the Fe(III) oxidation state (Figure S38). This is consistent with the increased amount of H_2O_2 production observed by RRDE under electrochemical conditions, since the two-electron/two-proton intermediate has time to diffuse away from the electrode where Fe(II) species capable of H_2O_2 reduction are generated. Alternatively, **5** can undergo a 2 e^- reduction and protonation of the distal O, leading to the release of water and formation of the stable Fe(III)−OH species, **6**. Stoichiometric experiments with Fe^{II}(PMG)Cl lead to quantitative oxidation by H_2O_2 to Fe(III) (Figure S37), which is supported by supplemental control studies with Fe(PMG)(Cl)$_2$ with added TBAOH (Figure 6). UV−vis data suggest that exposure of Fe^{II}(PMG)Cl to O_2 also leads to the formation of **6**; overlays of the product generated from Fe^{II}(PMG)Cl following exposure to O_2 or H_2O_2 show almost identical spectra (Figure 6). We propose that the dimer species decomposes to form species **6** under noncatalytic conditions by scavenging protons and H atom equivalents from solution. Following one-electron reduction, the terminal hydroxide ligand in complex **6** is then protonated to release one equivalent of water and complete the catalytic cycle.

Mechanistic studies with H_2O_2 demonstrate rapid catalytic reduction to H_2O occurs under these conditions only with Cp^*_2Fe present. The catalytic rate law implies an Fe(III)−OH resting state with first-order dependencies on [Fe(PMG)(Cl)$_2$] and [AcOH]. Based on spectroscopic analysis, we propose that H_2O_2 rapidly binds to complex **2**, which releases 1 equiv of water upon protonation to form the oxidized **6**, the resting state during H_2O_2RR. Consistent with the greater rates observed for H_2O_2RR than ORR spectrochemically, the electrochemically determined second-order rate constant for H_2O_2 binding, k_{H2O2} = 1.52 ± 0.16 × 10^3 M^{-1} s^{-1}, is 2 orders of magnitude greater than that for O_2 binding with AcOH present, $k_{O2,H+}$ = 6.12 ± 0.96 M^{-1} s^{-1}. Overall, the electrochemical and spectrochemical product analysis and mechanistic studies described above imply a 2+2 mechanistic pathway, where H_2O_2 is an intermediate in the catalytic cycle that is rapidly reduced to H_2O.

CONCLUSIONS

These data suggest that the bioinspired Fe(PMG)(Cl)$_2$ complex is an active and selective molecular catalyst for the reduction of O_2 to H_2O. Mechanistic studies support the existence of an off-cycle bridging diiron peroxo dimer, whose cleavage is rate-limiting. Additionally, the Fe(PMG)(Cl)$_2$ complex is also active for the catalytic reduction of H_2O_2, suggesting that the observed selectivity for water arises from an overall 2+2 mechanistic pathway. This proposal is supported by the observation of higher H_2O_2 efficiencies by RRDE, where hydrodynamic conditions push the two-electron/two-proton product away from sufficiently reducing conditions. The kinetic parameters of H_2O_2 reduction are consistent with a Fe(III)-hydroxide resting state, which was spectroscopically observed, indicating that this system could serve as a viable reactivity model for the O_2-driven oxidation reactions non-heme Fe metalloenzymes. Further, the observation of non-covalent interactions with the AcOH proton donor tuning the second-order rate constant of O_2 binding suggests that the electronic structure of the activated catalyst can be tuned via the carboxylate moiety. The role of anionic residues and their

https://doi.org/10.1021/jacs.1c04572
J. Am. Chem. Soc. XXXX, XXX, XXX−XXX

protonation state in regulating the reduction potentials at active sites has clear implications for a wide range of bioinorganic catalytic processes. Studies investigating the consequences of this ORR behavior on catalytic oxidation reactions and improving the ligand framework through synthetic modifications are currently underway.

■ ASSOCIATED CONTENT

Supporting Information

The Supporting Information is available free of charge at https://pubs.acs.org/doi/10.1021/jacs.1c04572.

Synthetic summaries, NMR and UV−vis characterization, electrochemistry, and description of experimental details and methods (PDF)

Computational coordinates (XYZ)

Accession Codes

CCDC 2080838−2080839 and 2103084 contain the supplementary crystallographic data for this paper. These data can be obtained free of charge via www.ccdc.cam.ac.uk/data_request/cif, or by emailing data_request@ccdc.cam.ac.uk, or by contacting The Cambridge Crystallographic Data Centre, 12 Union Road, Cambridge CB2 1EZ, UK; fax: +44 1223 336033.

■ AUTHOR INFORMATION

Corresponding Author

Charles W. Machan − *Department of Chemistry, University of Virginia, Charlottesville, Virginia 22904-4319, United States;* orcid.org/0000-0002-5182-1138; Email: machan@virginia.edu

Authors

Emma N. Cook − *Department of Chemistry, University of Virginia, Charlottesville, Virginia 22904-4319, United States;* orcid.org/0000-0002-0568-3600

Diane A. Dickie − *Department of Chemistry, University of Virginia, Charlottesville, Virginia 22904-4319, United States;* orcid.org/0000-0003-0939-3309

Complete contact information is available at: https://pubs.acs.org/10.1021/jacs.1c04572

Author Contributions

The manuscript was written through the contribution of all authors.

Funding

We thank the University of Virginia for infrastructural support. E.N.C. and C.W.M. acknowledge NSF CHE-2102156 and ACS PRF 61430-ND3 for support. Single-crystal X-ray diffraction experiments were performed on a diffractometer at the University of Virginia funded by the NSF-MRI program (CHE-2018870).

Notes

The authors declare no competing financial interest.

■ REFERENCES

(1) Pegis, M. L.; Wise, C. F.; Martin, D. J.; Mayer, J. M. Oxygen Reduction by Homogeneous Molecular Catalysts and Electrocatalysts. *Chem. Rev.* **2018**, *118* (5), 2340−2391.

(2) Machan, C. W. Advances in the Molecular Catalysis of Dioxygen Reduction. *ACS Catal.* **2020**, *10* (4), 2640−2655.

(3) Yoshikawa, S.; Shimada, A. Reaction Mechanism of Cytochrome c Oxidase. *Chem. Rev.* **2015**, *115* (4), 1936−1989.

(4) Denisov, I. G.; Makris, T. M.; Sligar, S. G.; Schlichting, I. Structure and Chemistry of Cytochrome P450. *Chem. Rev.* **2005**, *105* (6), 2253−2277.

(5) Shao, M.; Chang, Q.; Dodelet, J. P.; Chenitz, R. Recent Advances in Electrocatalysts for Oxygen Reduction Reaction. *Chem. Rev.* **2016**, *116* (6), 3594−3657.

(6) Sahu, S.; Goldberg, D. P. Activation of Dioxygen by Iron and Manganese Complexes: A Heme and Nonheme Perspective. *J. Am. Chem. Soc.* **2016**, *138* (36), 11410−11428.

(7) Campos-Martin, J. M.; Blanco-Brieva, G.; Fierro, J. L. G. Hydrogen Peroxide Synthesis: An Outlook beyond the Anthraquinone Process. *Angew. Chem., Int. Ed.* **2006**, *45* (42), 6962−6984.

(8) Pegis, M. L.; Martin, D. J.; Wise, C. F.; Brezny, A. C.; Johnson, S. I.; Johnson, L. E.; Kumar, N.; Raugei, S.; Mayer, J. M. Mechanism of Catalytic O2 Reduction by Iron Tetraphenylporphyrin. *J. Am. Chem. Soc.* **2019**, *141* (20), 8315−8326.

(9) Lu, X.; Lee, Y. M.; Sankaralingam, M.; Fukuzumi, S.; Nam, W. Catalytic Four-Electron Reduction of Dioxygen by Ferrocene Derivatives with a Nonheme Iron(III) TAML Complex. *Inorg. Chem.* **2020**, *59* (24), 18010−18017.

(10) Wang, Y. H.; Pegis, M. L.; Mayer, J. M.; Stahl, S. S. Molecular Cobalt Catalysts for O2 Reduction: Low-Overpotential Production of H2O2 and Comparison with Iron-Based Catalysts. *J. Am. Chem. Soc.* **2017**, *139* (46), 16458−16461.

(11) McGuire, R.; Dogutan, D. K.; Teets, T. S.; Suntivich, J.; Shao-Horn, Y.; Nocera, D. G. Oxygen Reduction Reactivity of Cobalt(II) Hangman Porphyrins. *Chem. Sci.* **2010**, *1* (3), 411−414.

(12) Lieske, L. E.; Hooe, S. L.; Nichols, A. W.; Machan, C. W. Electrocatalytic Reduction of Dioxygen by Mn(III): Mes-Tetra(N-Methylpyridinium-4-Yl)Porphyrin in Universal Buffer. *Dalt. Trans.* **2019**, *48* (24), 8633−8641.

(13) Passard, G.; Dogutan, D. K.; Qiu, M.; Costentin, C.; Nocera, D. G. Oxygen Reduction Reaction Promoted by Manganese Porphyrins. *ACS Catal.* **2018**, *8* (9), 8671−8679.

(14) Collman, J. P.; Boulatov, R.; Sunderland, C. J.; Fu, L. Functional Analogues of Cytochrome c Oxidase, Myoglobin, and Hemoglobin. *Chem. Rev.* **2004**, *104* (2), 561−588.

(15) Zhang, W.; Lai, W.; Cao, R. Energy-Related Small Molecule Activation Reactions: Oxygen Reduction and Hydrogen and Oxygen Evolution Reactions Catalyzed by Porphyrin- and Corrole-Based Systems. *Chem. Rev.* **2017**, *117* (4), 3717−3797.

(16) Jones, R. D.; Summerville, D. A.; Basolo, F. Synthetic Oxygen Carriers Related to Biological Systems. *Chem. Rev.* **1979**, *79* (2), 139−179.

(17) Kim, E.; Chufán, E. E.; Kamaraj, K.; Karlin, K. D. Synthetic Models for Heme-Copper Oxidases. *Chem. Rev.* **2004**, *104* (2), 1077−1133.

(18) Fukuzumi, S.; Lee, Y. M.; Nam, W. Mechanisms of Two-Electron versus Four-Electron Reduction of Dioxygen Catalyzed by Earth-Abundant Metal Complexes. *ChemCatChem* **2018**, *10* (1), 9−28.

(19) Nichols, A. W.; Kuehner, J. S.; Huffman, B. L.; Miedaner, P. R.; Dickie, D. A.; Machan, C. W. Reduction of Dioxygen to Water by a Co(N2O2) Complex with a 2,2′-Bipyridine Backbone. *Chem. Commun.* **2021**, *57*, 516−519.

(20) Wada, T.; Maki, H.; Imamoto, T.; Yuki, H.; Miyazato, Y. Four-Electron Reduction of Dioxygen Catalysed by Dinuclear Cobalt Complexes Bridged by Bis(Terpyridyl)Anthracene. *Chem. Commun.* **2013**, *49* (39), 4394−4396.

(21) Fukuzumi, S.; Kotani, H.; Lucas, H. R.; Doi, K.; Suenobu, T.; Peterson, R. L.; Karlin, K. D. Mononuclear Copper Complex-Catalyzed Four-Electron Reduction of Oxygen. *J. Am. Chem. Soc.* **2010**, *132* (20), 6874−6875.

(22) Kakuda, S.; Peterson, R. L.; Ohkubo, K.; Karlin, K. D.; Fukuzumi, S. Enhanced Catalytic Four-Electron Dioxygen (O2) and Two-Electron Hydrogen Peroxide (H2O2) Reduction with a Copper(II) Complex Possessing a Pendant Ligand Pivalamido Group. *J. Am. Chem. Soc.* **2013**, *135* (17), 6513−6522.

(23) Hooe, S. L.; Machan, C. W. Dioxygen Reduction to Hydrogen Peroxide by a Molecular Mn Complex: Mechanistic Divergence between Homogeneous and Heterogeneous Reductants. *J. Am. Chem. Soc.* **2019**, *141* (10), 4379−4387.
(24) Gennari, M.; Brazzolotto, D.; Pécaut, J.; Cherrier, M. V.; Pollock, C. J.; Debeer, S.; Retegan, M.; Pantazis, D. A.; Neese, F.; Rouzières, M.; Clérac, R.; Duboc, C. Dioxygen Activation and Catalytic Reduction to Hydrogen Peroxide by a Thiolate-Bridged Dimanganese(II) Complex with a Pendant Thiol. *J. Am. Chem. Soc.* **2015**, *137* (26), 8644−8653.
(25) Hooe, S. L.; Cook, E. N.; Reid, A. G.; Machan, C. W. Non-Covalent Assembly of Proton Donors and p- Benzoquinone Anions for Co-Electrocatalytic Reduction of Dioxygen. *Chem. Sci.* **2021**, *12* (28), 9733−9741.
(26) Wang, L.; Gennari, M.; Cantu Reinhard, F. G.; Gutierrez, J.; Morozan, A.; Philouze, C.; Demeshko, S.; Artero, V.; Meyer, F.; de Visser, S. P.; Duboc, C. A Non-Heme Diiron Complex for (Electro)Catalytic Reduction of Dioxygen: Tuning the Selectivity through Electron Delivery. *J. Am. Chem. Soc.* **2019**, *141* (20), 8244−8253.
(27) Ward, A. L.; Elbaz, L.; Kerr, J. B.; Arnold, J. Nonprecious Metal Catalysts for Fuel Cell Applications: Electrochemical Dioxygen Activation by a Series of First Row Transition Metal Tris(2-Pyridylmethyl)Amine Complexes. *Inorg. Chem.* **2012**, *51* (8), 4694−4706.
(28) Solomon, E. I.; Goudarzi, S.; Sutherlin, K. D. O2 Activation by Non-Heme Iron Enzymes. *Biochemistry* **2016**, *55* (46), 6363−6374.
(29) Costas, M.; Mehn, M. P.; Jensen, M. P.; Que, L. Dioxygen Activation at Mononuclear Nonheme Iron Active Sites: Enzymes, Models, and Intermediates. *Chem. Rev.* **2004**, *104* (2), 939−986.
(30) Kovaleva, E. G.; Lipscomb, J. D. Versatility of Biological Non-Heme Fe(II) Centers in Oxygen Activation Reactions. *Nat. Chem. Biol.* **2008**, *4* (3), 186−193.
(31) Feig, A. L.; Lippard; Stephen, J. Reactions of Non-Heme Iron(II) Centers with Dioxygen in Biology and Chemistry. *Chem. Rev.* **1994**, *94* (3), 759−805.
(32) Que, L.; Ho, R. Y. N. Dioxygen Activation by Enzymes with Mononuclear Non-Heme Iron Active Sites. *Chem. Rev.* **1996**, *96* (7), 2607−2624.
(33) Viggiani, A.; Siani, L.; Notomista, E.; Birolo, L.; Pucci, P.; Di Donato, A. The Role of the Conserved Residues His-246, His-199, and Tyr-255 in the Catalysis of Catechol 2,3-Dioxygenase from Pseudomonas Stutzeri OX1. *J. Biol. Chem.* **2004**, *279* (47), 48630−48639.
(34) Abu-Omar, M. M.; Loaiza, A.; Hontzeas, N. Reaction Mechanisms of Mononuclear Non-Heme Iron Oxygenases. *Chem. Rev.* **2005**, *105* (6), 2227−2252.
(35) Viswanathan, R.; Palaniandavar, M.; Balasubramanian, T.; Muthiah, T. P. Functional Models for Catechol 1,2-Dioxygenase. Synthesis, Structure, Spectra, and Catalytic Activity of Certain Tripodal Iron(III) Complexes. *Inorg. Chem.* **1998**, *37* (12), 2943−2951.
(36) Cox, D. D.; Que, L. Functional Models for Catechol 1,2-Dioxygenaes. The Role of the Iron(III) Center. *J. Am. Chem. Soc.* **1988**, *110* (24), 8085−8092.
(37) Velusamy, M.; Mayilmurugan, R.; Palaniandavar, M. Iron(III) Complexes of Sterically Hindered Tetradentate Monophenolate Ligands as Functional Models for Catechol 1,2-Dioxygenases: The Role of Ligand Stereoelectronic Properties. *Inorg. Chem.* **2004**, *43* (20), 6284−6293.
(38) Li, F.; Wang, M.; Li, P.; Zhang, T.; Sun, L. Iron(III) Complexes with a Tripodal N3O Ligand Containing an Internal Base as a Model for Catechol Intradiol-Cleaving Dioxygenases. *Inorg. Chem.* **2007**, *46* (22), 9364−9371.
(39) Visvaganesan, K.; Mayilmurugan, R.; Suresh, E.; Palaniandavar, M. Iron(III) Complexes of Tridentate 3N Ligands as Functional Models for Catechol Dioxygenases: The Role of Ligand N-Alkyl Substitution and Solvent on Reaction Rate and Product Selectivity. *Inorg. Chem.* **2007**, *46* (24), 10294−10306.
(40) Schmidt, S. B.; Husted, S. The Biochemical Properties of Manganese in Plants. *Plants* **2019**, *8* (10), 381−395.
(41) Banerjee, S. R.; Wei, L.; Levadala, M. K.; Lazarova, N.; Golub, V. O.; O'Connor, C. J.; Stephenson, K. A.; Valliant, J. F.; Babich, J. W.; Zubieta, J. {Re(III)(Cl)3} Core Complexes with Bifunctional Single Amino Acid Chelates. *Inorg. Chem.* **2002**, *41* (22), 5795−5802.
(42) Piguet, C. Paramagnetic Susceptibility by NMR: The "Solvent Correction" Removed for Large Paramagnetic Molecules. *J. Chem. Educ.* **1997**, *74* (7), 815−816.
(43) Bain, G. A.; Berry, J. F. Diamagnetic Corrections and Pascal's Constants. *J. Chem. Educ.* **2008**, *85* (4), 532−536.
(44) Hooe, S. L.; Rheingold, A. L.; Machan, C. W. Electrocatalytic Reduction of Dioxygen to Hydrogen Peroxide by a Molecular Manganese Complex with a Bipyridine-Containing Schiff Base Ligand. *J. Am. Chem. Soc.* **2018**, *140* (9), 3232−3241.
(45) Nichols, A. W.; Chatterjee, S.; Sabat, M.; Machan, C. W. Electrocatalytic Reduction of CO2 to Formate by an Iron Schiff Base Complex. *Inorg. Chem.* **2018**, *57* (4), 2111−2121.
(46) Mandon, D.; Machkour, A.; Goetz, S.; Welter, R. Trigonal Bipyramidal Geometry and Tridentate Coordination Mode of the Tripod in FeCl2 Complexes with Tris(2-Pyridylmethyl)Amine Derivatives Bis-α-Substituted with Bulky Groups. Structures and Spectroscopic Comparative Studies. *Inorg. Chem.* **2002**, *41* (21), 5364−5372.
(47) Savéant, J.-M.; Costentin, C. Chapter 2 Coupling of the Electrode Electron Transfers with Homogeneous Chemical Reactions. In *Elements of Molecular and Biomolecular Electrochemistry: An Electrochemical Approach to Electron Transfer Chemistry*; John Wiley & Sons, Inc.: Hoboken, NJ, 2019; pp 78−179.
(48) Zanello, P. Chapter 2 Voltammetric Techniques. In *Inorganic Electrochemistry: Theory, Practice and Application*; The Royal Society of Chemistry: Cambridge, UK, 2003; pp 49−135.
(49) Elgrishi, N.; Kurtz, D. A.; Dempsey, J. L. Reaction Parameters Influencing Cobalt Hydride Formation Kinetics: Implications for Benchmarking H2-Evolution Catalysts. *J. Am. Chem. Soc.* **2017**, *139* (1), 239−244.
(50) McCarthy, B. D.; Martin, D. J.; Rountree, E. S.; Ullman, A. C.; Dempsey, J. L. Electrochemical Reduction of Brønsted Acids by Glassy Carbon in Acetonitrile-Implications for Electrocatalytic Hydrogen Evolution. *Inorg. Chem.* **2014**, *53* (16), 8350−8361.
(51) Matsubara, Y. Unified Benchmarking of Electrocatalysts in Noninnocent Second Coordination Spheres for CO2 Reduction. *ACS Energy Lett.* **2019**, *4* (8), 1999−2004.
(52) Anson, C. W.; Stahl, S. S. Cooperative Electrocatalytic O2 Reduction Involving Co(Salophen) with p-Hydroquinone as an Electron-Proton Transfer Mediator. *J. Am. Chem. Soc.* **2017**, *139* (51), 18472−18475.
(53) Burés, J. A Simple Graphical Method to Determine the Order in Catalyst. *Angew. Chem., Int. Ed.* **2016**, *55* (6), 2028−2031.
(54) F. van Strijdonck, G. P.; Boele, M. D. K.; Kamer, P. C. J.; de Vries, J. G.; van Leeuwen, P. W. N. M. Fast Palladium Catalyzed Arylation of Alkenes Using Bulky Monodentate Phosphorus Ligands. *Eur. J. Inorg. Chem.* **1999**, *1999* (7), 1073−1076.
(55) Brunold, T. C.; Tamura, N.; Kitajima, N.; Moro-Oka, Y.; Solomon, E. I. Spectroscopic Study of [Fe2(O2)(OBz)2{HB(Pz′)-3}2]: Nature of the μ-1,2 Peroxide-Fe(III) Bond and Its Possible Relevance to O2 Activation by Non-Heme Iron Enzymes. *J. Am. Chem. Soc.* **1998**, *120* (23), 5674−5690.
(56) Feig, A. L.; Masschelein, A.; Bakac, A.; Lippard, S. J. Kinetic Studies of Reactions of Dioxygen with Carboxylate-Bridged Diiron(II) Complexes Leading to the Formation of (μ-Oxo)Diiron(III) Complexes. *J. Am. Chem. Soc.* **1997**, *119* (2), 334−342.
(57) Dong, Y.; Zang, Y.; Shu, L.; Wilkinson, E. C.; Que, L.; Kauffmann, K.; Münck, E. Models for Nonheme Diiron Enzymes. Assembly of a High-Valent Fe 2 (μ-O) 2 Diamond Core from Its Peroxo Precursor. *J. Am. Chem. Soc.* **1997**, *119* (51), 12683−12684.

https://doi.org/10.1021/jacs.1c04572
J. Am. Chem. Soc. XXXX, XXX, XXX−XXX